Fabricating lifted Haar transform image compression optical chip based on femtosecond laser*

TAO Qing[1,2], WEI Liangpeng[1], KUANG Wenxiang[1], YIN Yegang[1], CHENG Jian[1], and LIU Dun[1]**

1. Laser Group, School of Mechanical Engineering, Hubei University of Technology, Wuhan 430068, China

2. Hubei Key Laboratory of Modern Manufacturing Quantity Engineering, School of Mechanical Engineering, Hubei University of Technology, Wuhan 430068, China

(Received 16 February 2023; Revised 19 April 2023)

In this paper, a lifted Haar transform (LHT) image compression optical chip has been researched to achieve rapid image compression. The chip comprises 32 same image compression optical circuits, and each circuit contains a 2×2 multimode interference (MMI) coupler and a π/2 delay line phase shifter as the key components. The chip uses highly borosilicate glass as the substrate, Su8 negative photoresist as the core layer, and air as the cladding layer. Its horizontal and longitudinal dimensions are 8 011 μm×10 000 μm. Simulation results present that the designed optical circuit has a coupling ratio (*CR*) of 0: 100 and an insertion loss (*IL*) of 0.001 548 dB. Then the chip is fabricated by femtosecond laser and testing results illustrate that the chip has a *CR* of 6: 94 and an *IL* of 0.518 dB. So, the prepared chip possesses good image compression performance.

Document code: A **Article ID:** 1673-1905(2023)09-0519-7

DOI https://doi.org/10.1007/s11801-023-3023-z

Rapid development of digital media has made a variety of images at present, the demands for higher storage capabilities and faster computing speeds are increasing. Image compression can be achieved by reducing redundant information because an image is made up of some interrelated pixels[1]. The most common methods for image compression are discrete Fourier transform (DFT), discrete cosine transform (DCT), and discrete wavelet transform (DWT). DWT is optimal choice because it can overcome the limitations of DFT and DCT when to analyze input signals at different scales and resolutions[2,3].

Compared with electronic systems, optical chips have received worldwide attention recently because they have conquered the shortcomings of optical-to-electrical-to-optical (OEO) transformation. As carriers of information interaction between computing units, photons have advantages of high transmission speed and anti-interference ability[4], therefore, optical chips have more powerful optical processing capabilities as well as flexibility and reconfigurability[5], they are multi-channel devices with optical waveguides embedded into them.

Silicon, silicon oxynitride, indium phosphide, lithium niobate, gallium arsenide, and polymers all can be implemented on optical chips[6-11]. As a polymer material, Su8 negative photoresist has good compatibility with substrate, and it is more suitable for mass production[12]. Femtosecond laser has ultra-short pulse width and ultra-high instantaneous power to achieve ultra-high precision micro-nano machining, its heat-affected area is small enough. Femtosecond laser can process various materials, it is a new fabricating method for optical waveguides and its machining steps are less than that of lithography technology, which has improved the processing efficiency[13]. This paper presented a 64-channel lifted Haar transform (HT) image compression optical chip that fabricated by femtosecond laser with Su8 negative photoresist core.

HT is the simplest discrete wavelet transform, which is a mathematical operation based on Haar wavelet which can be used to achieve image compression by ignoring unimportant parts of the transform domain. Besides HT, other more powerful wavelet transforms can also be used for image compression, but it should be considered that HT is easier to be implemented because of its simple structure and feature of easily being used to perform simple manual calculations[14,15]. In this study, improvement has been made to HT so that it has faster efficiency when applied to image compression.

Lifted Haar transform (LHT) decomposes a pixel value matrix into two sub-matrices with a length equal to half of the original matrix. One sub-matrix is a running difference or fluctuation, the other is a running average or trend. For the pixel value matrix $\boldsymbol{p}$ with a length of N,

* This work has been supported by the Natural Science Foundation of Hubei Province (No.2017CFB685), Hubei University of Technology "Advanced Manufacturing Technology and Equipment" Collaborative Innovation Center Open Research Fund (Nos.038/1201501 and 038/1201803), and the College-level Project of Hubei University of Technology (Nos.4201/01758, 4201/01802, 4201/01889, and 4128/21025).

** E-mail: dun.liu@hbut.edu.cn

the first difference sub-matrix $\boldsymbol{d}^1$ and the first average sub-matrix $\boldsymbol{a}^1$ are obtained, respectively by

$$\boldsymbol{p}=(p_1,\ p_2,...,\ p_N),\tag{1}$$

$$\boldsymbol{d}^1=(d_1,\ d_2,...,\ d_{N/2}),\tag{2}$$

$$\boldsymbol{a}^1=(a_1,\ a_2,...,\ a_{N/2}),\tag{3}$$

$$d_m=\frac{p_{2m-1}-2\sqrt{p_{2m-1}p_{2m}}+p_{2m}}{2},\tag{4}$$

$$a_m=\frac{p_{2m-1}+2\sqrt{p_{2m-1}p_{2m}}+p_{2m}}{2},\tag{5}$$

where m=1, 2, 3, …, N/2. p_1, p_2, …, p_N represent the pixel values of the original image, while d_m and a_m represent the pixel values of the transformed image, and compression is realized by reserving a_m while neglecting d_m. Establishing a one-to-one mapping between pixel values and optical power which can be directly transformed by the chip, which would eliminate the steps of converting the signal values to power values and the power values to signal values since $d_m+a_m=p_{2m-1}+p_{2m}$, which mathematically shortens length of the transformation matrix and makes the transformation easier and faster.

LHT can be performed at different levels, and the first level is defined as

$$\boldsymbol{p}\xrightarrow{\text{LHT}}(\boldsymbol{d}^1,\boldsymbol{a}^1)=\{\frac{p_1-2\sqrt{p_1p_2}+p_2}{2},\ \frac{p_1+2\sqrt{p_1p_2}+p_2}{2},...,\frac{p_{N/2-1}-2\sqrt{p_{N/2-1}p_{N/2}}+p_{N/2}}{2},\ \frac{p_{N/2-1}+2\sqrt{p_{N/2-1}p_{N/2}}+p_{N/2}}{2}\}.\tag{6}$$

By applying the process used for obtaining first level LHT on the average sub-matrix, higher orders of LHT could be achieved[16].

Key components of the image compression optical circuit are multimode interference (MMI) coupler and π/2 delay line phase shifter[17,18]. In the optical circuit, π/2 delay line phase shifter provides a constant phase difference for the two input signals. After interference and superposition in the MMI, substraction and sum signals are obtained in the outputs. The compression can be achieved through considering the sum signal and eliminating the subtraction signal.

MMI has the advantages of compact structure, easy to prepare, low loss, good production tolerance and small polarization correlation, etc. Two-dimensional structure of the MMI is presented in Fig.1. It can support m waveguide propagation modes at wavelength λ_0=1 550 nm, ν=0, 1, 2, …, (m−1) denotes orders of different modes. The light field propagating along Z-axis in the MMI is a linear superposition of all guided modes, and the field profile at a distance L can be written as

$$F(x,L)=\sum_{\nu=0}^{\nu=m-1}c_\nu f_\nu(x)\exp\left[\mathrm{i}\frac{\nu(\nu+2)\pi}{3L_\pi}L\right],\tag{7}$$

where c_ν is field excitation coefficient, $f_\nu(x)$ is ν order local mode of the MMI, L_π is beating length of the two lowest-order modes, $\exp\left[\mathrm{i}\frac{\nu(\nu+2)\pi}{3L_\pi}L\right]=(-1)^{\frac{\nu(\nu+2)}{3L_\pi}L}$ is phase factor of the ν order mode, and $F(x, L)$ will be an image of $F(x, 0)$ if $\exp\left[\mathrm{i}\frac{\nu(\nu+2)\pi}{3L_\pi}L\right]=1$ or $\exp\left[\mathrm{i}\frac{\nu(\nu+2)\pi}{3L_\pi}L\right]=(-1)\nu(\nu+2)$.

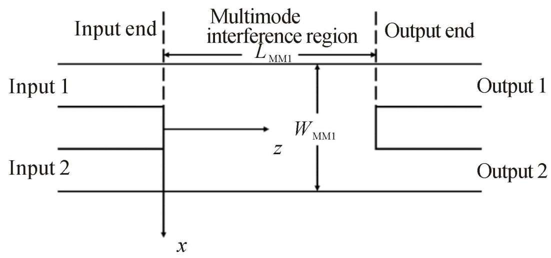

Fig.1 Two-dimensional structure of the MMI

In the above, first condition means that phase changes of all modes along L must differ by integer multiples of 2π, the image is a direct replica of the input light field. Second condition means that phase changes must be alternatively even and odd multiples of π, the interference produces an image mirrored to the input light field.

For $L=p(3L_\pi)$, p is non-negative integer, $\exp\left[\mathrm{i}\frac{\nu(\nu+2)}{3L_\pi}L\right]=(-1)p\nu(\nu+2)$. When p is even, $(-1)p\nu(\nu+2)=1$, the image is a direct replica of the input light field. When p is odd, $\begin{cases}p\nu(\nu+2)=\text{even} & \nu=\text{even}\\ p\nu(\nu+2)=\text{odd} & \nu=\text{odd}\end{cases}$, the phase changes must be alternatively even and odd multiples of π, the interference produces an image mirrored to the input light field.

Considering the images obtained half way between the direct and mirrored image positions, $L=p(3L_\pi)/2$, p is non-negative integer, and the light field at these distances is indicated as

$$F(x,\frac{p}{2}3L_\pi)=\sum_{\nu=0}^{\nu=m-1}c_\nu f_\nu\exp[\mathrm{i}\nu(\nu+2)p(\frac{\pi}{2})].\tag{8}$$

That is

$$F(x,\frac{p}{2}3L_\pi)=\frac{1+(-\mathrm{i})^p}{2}F(x,0)+\frac{1-(-\mathrm{i})^p}{2}F(-x,0),\tag{9}$$

which represents a pair of symmetrical images of $F(x,0)$, in quadrature and with amplitudes $1/\sqrt{2}$, at $z=\frac{1}{2}(3L_\pi)$, $z=\frac{3}{2}(3L_\pi)$,… .

For the structure compactness, p=1 is taken. As presented in Fig.2, when $L_{\mathrm{MMI}}=\frac{3}{2}L_{\pi}$, the input light field will be divided into two fields with same amplitudes $1/\sqrt{2}$ and phase difference of $\pi/2$ in output 1 and output 2. Similarly, the other light field will be divided into two fields with same amplitudes $1/\sqrt{2}$ and phase difference of $-\pi/2$ in output 1 and output 2. Because $\pi/2$ delay line phase shifter provides a constant phase difference $\pi/2$ for the two input light fields, after interference and superposition, a phase difference of π will be formed at output 1, the amplitude of total field at output 1 will be 0 theoretically, and a phase difference of 0 is formed at output 2, and the amplitude of total field at output 2 will be $\sqrt{2}$.

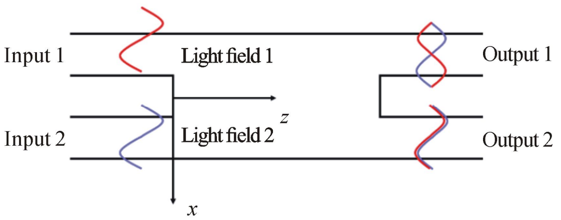

Fig.2 Interference and superposition of the light fields in the MMI

According to the relationship between amplitude and power, when the optical power of light field 1 and field 2 are P_1 and P_2, and they have an initial phase difference of $\pi/2$, the optical power at output 1 and 2 after MMI interference will be

$$P_1'=\frac{P_1-2\sqrt{P_1P_2}+P_2}{2},\quad P_2'=\frac{P_1+2\sqrt{P_1P_2}+P_2}{2}. \tag{10}$$

Structure of the image compression optical chip is shown in Fig.3, which is composed of 32 same image compression optical circuits. Each optical circuit is composed of a 2×2 MMI and a $\pi/2$ delay line phase shifter.

Substrate of the chip is highly borosilicate glass, refractive index n_s=1.47. The core layer is Su8 negative photoresist, refractive index n_r=1.569 34. Cross section of the core layer is 10 μm×10 μm. The cladding layer is air, refractive index n_c=1. Spacing of the adjacent input or output ports is 127 μm, the horizontal and longitudinal dimensions of the optical chip are 8 011 μm and 10 000 μm, and woking wavelength of the chip is λ_0=1 550 nm.

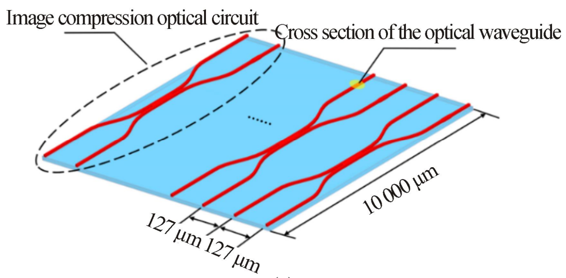

(a)

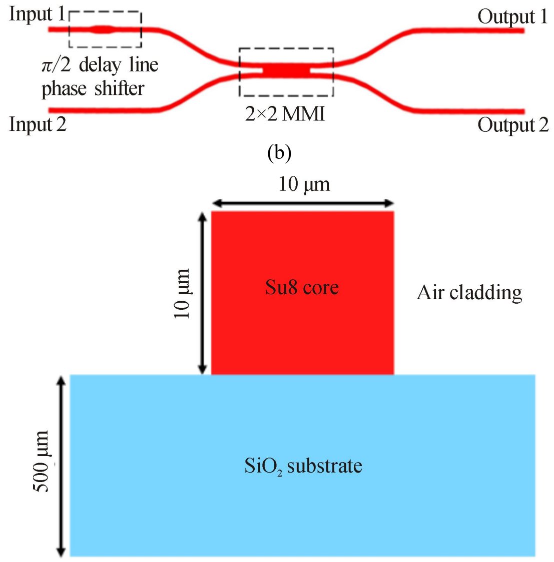

(b)

(c)

Fig.3 (a) Structure of the image compression optical chip; (b) Image compression optical circuit; (c) Cross section of the optical waveguide

Propagation loss of the MMI increases with its size, considering the laser machining accuracy at the same time, set W_{MMI}=30 μm, so its effective width is

$$W_e=W_{\mathrm{MMI}}+\delta W=W_{\mathrm{MMI}}+\left(\frac{\lambda_0}{\pi}\right)\left(\frac{n_c}{n_r}\right)^{2\sigma}\left(n_r^2-n_c^2\right)^{-\frac{1}{2}}, \tag{11}$$

where δW is penetrating depth. σ=0 (σ=0 for TE modes and σ=1 for TM modes) is taken into Eq.(11), W_e=30.407 93 μm and $L_{\mathrm{MMI}}=\frac{3}{2}L_{\pi}=\frac{3}{2}\times\frac{4n_rW_e^2}{3\lambda_0}=$ 1 872.359 μm can be obtained. Here, L_{MMI} is just a calculated value, in order to optimize the result, transmission field distribution in the MMI is simulated in software at different L_{MMI} values with a scanning range of 1 862—1 882 μm and a scanning step of 0.05 μm. Coupling ratio (CR) and insertion loss (IL)[19] of the MMI corresponding to different L_{MMI} values are shown in Fig.4.

$$CR=\frac{P_{\mathrm{output1}}}{P_{\mathrm{output2}}}, \tag{12}$$

$$IL=-10\lg\frac{P_{\mathrm{output1}}+P_{\mathrm{output2}}}{P_{\mathrm{input1}}+P_{\mathrm{intput2}}}. \tag{13}$$

Shift of the MMI length has little influence on CR which is always close to 0 in the scanning range. When L_{MMI}=1 871.55 μm, IL of the MMI reaches minimum of 0.001 526 dB, and the simulation result is presented in Fig.5.

Optimized sizes of the MMI obtained from the simulation results are 30 μm×1 871.55 μm, which is presented in Fig.6.

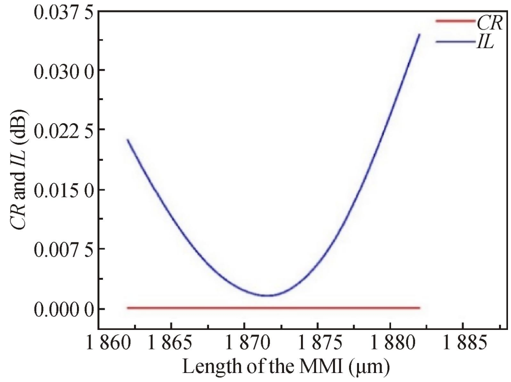

Fig.4 Effects of the MMI length shift on *CR* and *IL*

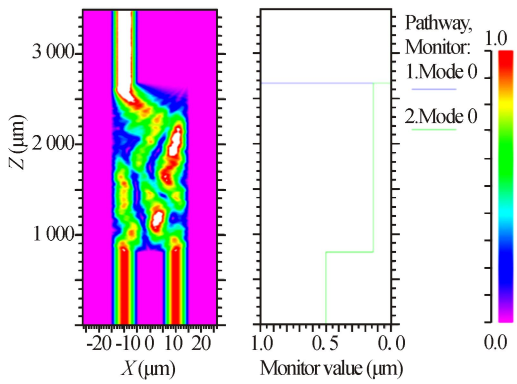

Fig.5 Simulation result when L_{MMI}=1 871.55 μm

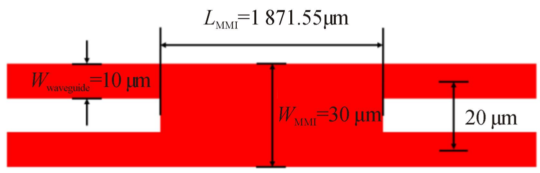

Fig.6 Optimized 2×2 MMI sizes

The phase shifter used in the image compression optical circuit consists of one rectangular optical waveguide and two symmetrically tapered optical waveguides that provide a phase difference of $\pi/2$ totally.

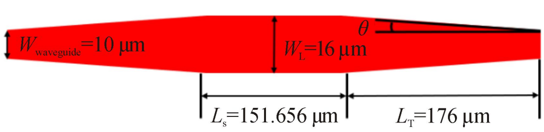

Fig.7 Structure of the π/2 delay line phase shifter

The rectangular optical waveguide provides a phase difference as

$$\Delta\varphi_R=\frac{\pi\lambda_0\left[\left(W_L+\delta W\right)^2-\left(W_{\text{waveguide}}+\delta W\right)^2\right]L_S}{4n_r\left(W_L+\delta W\right)^2\left(W_{\text{waveguide}}+\delta W\right)^2},\quad(14)$$

where W_L and L_S are width and length of the rectangular optical waveguide, $W_{\text{Waveguide}}$=10 μm is width of the single mode optical waveguide. Inclination of the tapered optical waveguide is

$$\tau=\tan\theta=\frac{W_L-W_{\text{waveguide}}}{2L_T}.\quad(15)$$

In the above equation, L_T is the taper length. Besides, the inclination τ needs to fulfill

$$\tau<\frac{3\left(W_{\text{waveguide}}+\delta W\right)\lambda_0}{4n_r\left(W_L+\delta W\right)^2}.\quad(16)$$

Taking Eq.(15) into Eq.(16), we can get

$$L_T>\frac{\left(W_L-10\right)\left(W_L+0.407\ 93\right)^2}{15.419\ 5}.\quad(17)$$

Considering the chip size and machining accuracy, take W_L=16 μm, so L_T>104.758 3 μm. Phase difference provided by one tapered optical waveguide is

$$\Delta\varphi_T=\frac{\pi\lambda_0}{4n_r}\times\left[\frac{L_T}{\left(W_{\text{waveguide}}+\delta W\right)^2}+\frac{1}{2\tau\left(W_L+\delta W\right)}-\frac{1}{2\tau\left(W_{\text{waveguide}}+\delta W\right)}\right].\quad(18)$$

Set the total phase difference as

$$\Delta\varphi_R+2\Delta\varphi_T=\frac{\pi}{2}.\quad(19)$$

Taking Eq.(14) and Eq.(18) into Eq.(19), we get

$$L_S=-1.223\ 748\ 184\ 842\ 9L_T+367.036\ 011\ 041\ 66.\quad(20)$$

It can be known that L_S is linearly related to L_T from Eq.(20). Similarly, set scanning range and scanning step of L_T as 170—190 μm and 0.05 μm, respectively, and *CR* and *IL* of the image compression optical circuit change with different L_T values are presented in Fig.8.

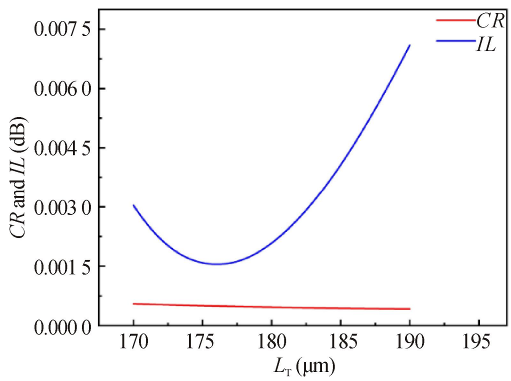

Fig.8 Effect of L_T shift on *CR* and *IL*

In the scanning range, *CR*≈0 constantly. When L_T=176 μm and L_S=151.656 μm, *IL* of the optical circuit reaches minimum of 0.001 548 dB, and simulation results are as follows.

Take a 30 mm×30 mm×0.5 mm highly borosilicate glass as the substrate, soak it in a beaker which contains 95% ethanol solution, and then place the beaker in an ultrasonic cleaner for 30 min. Next, take out the substrate and use nitrogen to blow it dry to ensure the surface of the substrate is clean. A spin coater is used to uniformly rotate the Su8 negative photoresist on the substrate and

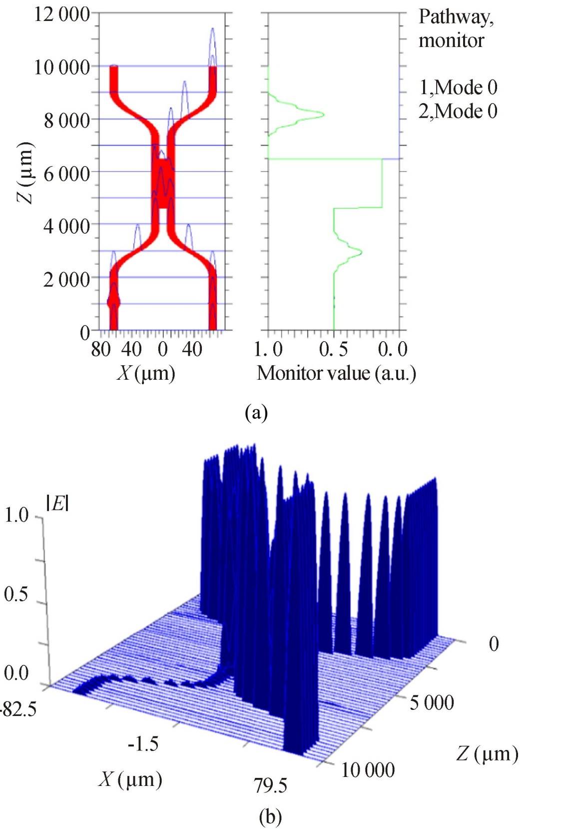

Fig.9 (a) Distribution of the optical power along transmission line; (b) Stereoscopic distribution of electrical vector amplitude in the direction of transmission line

thickness of the core layer is 10 μm. Above processes should be carried out in a vacuum operation box. Finally, put the sample in an oven and bake at 120 °C for 30 min, then, it is taken out for natural cooling. Femtosecond laser was used to prepare the chip with center wavelength of λ=800 nm, repetition rate of f=1 kHz, pulse width of 100 fs, single pulse energy of E_P<4.5 mJ, and beam factor of M^2<1.3. The femtosecond laser machining system is displayed in Fig.10, where the power attenuation system consists of a half wave plate (HWP) and a polarizing beam splitter (PBS), continuous adjustment of the laser machining power can be realized by turning the knob on the HWP. The mirror is used to change the beam path to focus the laser on the sample surface. Aerotech 6-Dof staging is controlled by computer program to achieve laser precise machining. The focusing objective is a 20× objective with a numerical aperture (*NA*) of 0.40. Theoretical spot diameter *D* at focal point of the objective lens is about 1.7 μm.

The minimum average machining power of a material refers to the minimum power density required for irreversible damage to the material to occur. Determination of the minimum average machining power can provide important guidance for subsequent machining. Femtosecond laser processing parameters and the material itself will affect the minimum average machining power. On this account, we can design experiment to explore the minimum average machining power of the Su8 photoresist.

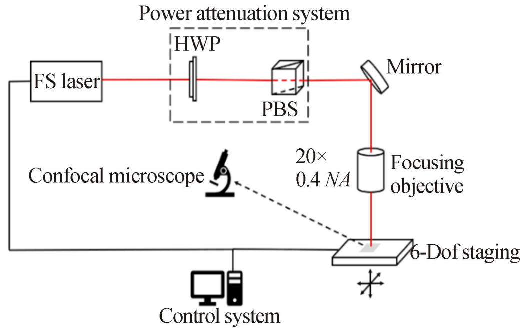

Fig.10 Femtosecond laser machining system

By machining the sample using femtosecond laser single pulse, measure average diameters of the damage areas at different machining power by a microscope.

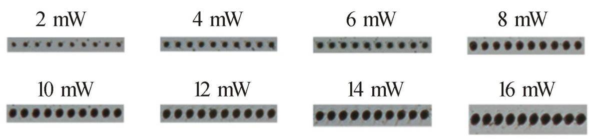

Fig.11 Machining effects of the femtosecond laser single pulse

Average diameters of the damage areas corresponding to different machining power are as follows.

The relationship among single pulse energy E_P, machining power P and repetition frequency f is

$$E_P = \frac{P}{f}. \tag{21}$$

And the relationship between diameter of the damage area D and single pulse energy E_P is

$$D^2 = 2\omega_0^2\left(\ln E_P + \ln\frac{2}{\pi\omega_0^2\varphi_{\rm th}}\right), \tag{22}$$

where ω_0 is femtosecond laser spot radius, and $\varphi_{\rm th}$ is damage threshold of the material. According to Eq.(22), $\ln E_P$ is linearly related to D^2, a linear fit is performed on the data in Tab.1, and the following function image is got.

Equation of the red line is

$$D^2 = -10.623\,46 + 26.091\,99\ln E_P, \tag{23}$$

where D=0 is the critical point of material damage. Substituting D=0 into Eq.(23), we can get $\ln E_P$=0.408 3, then the minimum average machining power P=1.504 mW can be calculated through taking $\ln E_P$=0.408 3 to Eq.(21).

In the experimental process, laser machining power and scanning speed are important factors that affect the machining effects. It is difficult to find out the optimal combination of the machining parameters if one of the parameters is controlled and studied individually by the control variable method. In view of the above, set the laser machining power and the scanning speed in variable ranges, and investigate the machining effects under different combinations of the two parameters by using the laser marking method[20]. When the laser machining power is 2 mW and the scanning speed is 4 mm/s, the machining error is the smallest and the machining quality is the best.

Tab.1 Average diameters of the damage areas corresponding to different machining power

Machining power (mW)	Average diameters of the damage areas (μm)
2	3.794
4	4.786
6	5.114
8	6.679
10	6.888
12	7.097
14	7.820
16	8.329

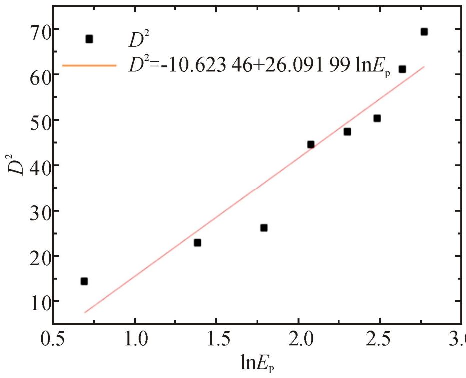

Fig.12 Relationship between *D* and *E*P

The chip fabricated by femtosecond laser is presented in Fig.13. In the figure, we can find out that macroscopic outline of the chip is clear, and microstructures of the MMI and the phase shifter observed under the confocal microscope meet the design requirements. Sizes of critical parts in the chip are close to the optimal values.

A testing system based on light source and single channel optical power meter is shown in Fig.14. The light source has a center wavelength of 1 550 nm and an optical power of 10 dBm. Light emitted from the light source enters 1×2 optical splitter through single mode fiber (SMF) which can ensure that the two beams of light entering the optical circuit to be measured have the same amplitude and phase. To minimize coupling loss, 6-axis high-precision trimmers and vision system are taken into the testing system. Use the single channel optical power meter that connected with the optical circuit by multi mode fiber (MMF) to measure the optical power of output 1 and output 2 of the optical circuit. Repeat the above steps, measure output 1 and output 2 optical power of the remaining 31 image compression optical circuits, take average of the optical power in output 1 and output 2, respectively, and then calculate *CR* and *IL* of the chip by Eqs.(12) and (13).

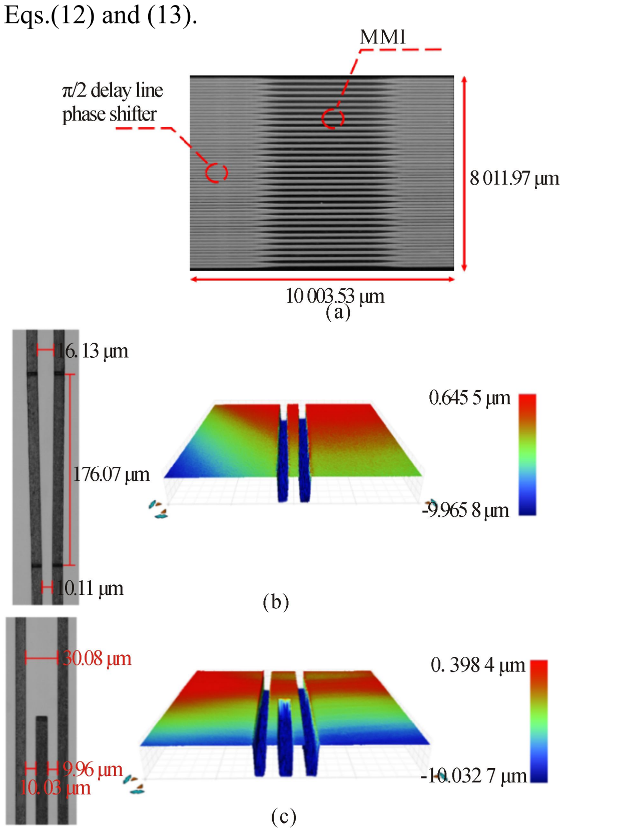

Fig.13 (a) Vertical view of the image compression optical chip; (b) Microstructure of the π/2 delay line phase shifter; (c) Microstructure of the MMI

Testing results presented that the image compression optical chip has a *CR* of 6: 94 and an *IL* of 0.518 dB. Consequently, the fabricated chip possesses acceptable image compression ability.

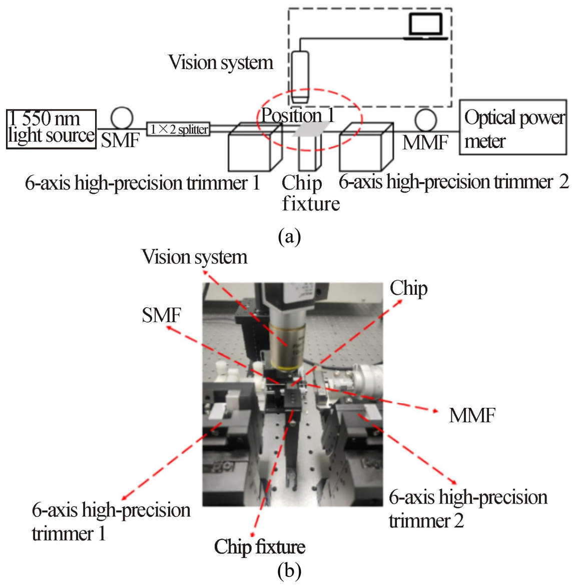

Fig.14 (a) The chip testing system; (b) Physical picture of position 1

In this paper, an LHT image compression optical chip has been designed and prepared, which uses Su8 negative photoresist (n_r=1.569 34) as core layer, high borosilicate glass (n_s=1.47) as substrate, and air (n_c=1) as cladding layer, and it works at λ_0=1 550 nm. Simulation results show that the chip can well limit the energy of the light field in the optical waveguide and *CR* of 0: 100, *IL* of 0.001 548 dB can be obtained, which meets the design requirements. Then the chip is prepared by femtosecond laser. A testing system is built to test the chip, and the results indicate *CR*=6: 94 and *IL*=0.518 dB, so the chip has an acceptable image compression capacity.

Ethics declarations

Conflicts of interest

The authors declare no conflict of interest.

References

[1] MISHRA D, SINGH S K, SINGH R K. Deep architectures for image compression：a critical review[J]. Signal processing, 2022, 191：108346.

[2] FARES K, KHALDI A, REDOUANE K, et al. DCT & DWT based watermarking scheme for medical information security[J]. Biomedical signal processing and control, 2021, 66：102403.

[3] FARES K, AMINE K, SALAH E. A robust blind color image watermarking based on Fourier transform domain[J]. Optik, 2020, 208：164562.

[4] MENG J, MISCUGLIO M, GEORGE J K, et al. Electronic bottleneck suppression in next-generation networks with integrated photonic digital-to-analog converters[J]. Advanced photonics research, 2021, 2(2)：2000033.

[5] ANAGHA E G, JEYACHITRA R K. Review on all-optical logic gates：design techniques and classifications-heading toward high-speed optical integrated circuits[J]. Optical engineering, 2022, 61(6)：060902.

[6] URBONAS D, MAHRT R F, STÖFERLE T. Low-loss optical waveguides made with a high-loss material[J]. Light：science & applications, 2021, 10(1)：15.

[7] SUDAS D P, ZAKHAROV L Y, JITOV V A, et al. Silicon oxynitride thin film coating to lossy mode resonance fiber-optic refractometer[J]. Sensors, 2022, 22(10)：3665.

[8] FRIDLANDER J, SANG F, ROSBOROUGH V, et al. Dual laser indium phosphide photonic integrated circuit for integrated path differential absorption lidar[J]. IEEE journal of selected topics in quantum electronics, 2021, 28(1)：1-8.

[9] YAO N, ZHOU J, GAO R, et al. Efficient light coupling between an ultra-low loss lithium niobate waveguide and an adiabatically tapered single mode optical fiber[J]. Optics express, 2020, 28(8)：12416-12423.

[10] EL-HAGEEN H M, ALATWI A M, RASHED A N Z. Silicon-germanium dioxide and aluminum indium gallium arsenide-based acoustic optic modulators[J]. Open engineering, 2020, 10(1)：506-511.

[11] BUZZIN A, ASQUINI R, CAPUTO D, et al. On-glass integrated SU-8 waveguide and amorphous silicon photosensor for on-chip detection of biomolecules：feasibility study on hemoglobin sensing[J]. Sensors, 2021, 21(2)：415.

[12] XU M, WU Q, WEI W, et al. Preparation and electrochemical application of an AgNW/graphene/SU-8 composite conductive photoresist[J]. Journal of applied polymer science, 2021, 138(41)：51205.

[13] HE J, XU B, XU X, et al. Review of femtosecond-laser-inscribed fiber Bragg gratings：fabrication technologies and sensing applications[J]. Photonic sensors, 2021, 11：203-226.

[14] BELYAEV A A, YEVTUSHOK O S, RYABOSHCHUK N M. Lossless image compression algorithm based on Haar transform[C]//2021 IEEE Conference of Russian Young Researchers in Electrical and Electronic Engineering (ElConRus), January 26-29, 2021, Moscow, Russia. New York：IEEE, 2021：1960-1964.

[15] LIU D, SU Q, YUAN Z, et al. A fusion-domain color image watermarking based on Haar transform and image correction[J]. Expert systems with applications, 2021, 170：114540.

[16] FASHI A A, SAMIEI M H V, TEIXEIRA A. Design of a visible light photonic chip for Haar transform based optical compression[J]. Optik, 2020, 217：164929.

[17] PÉREZ-ARMENTA C, ORTEGA-MOÑUX A, LUQUE-GONZÁLEZ J M, et al. Polarization-independent multimode interference coupler with anisotropy-engineered bricked metamaterial[J]. Photonics research, 2022, 10(4)：A57-A65.

[18] UNUTMAZ M A, UNLU M. Spoof surface plasmon polariton delay lines for terahertz phase shifters[J]. Journal of lightwave technology, 2021, 39(10)：3187-3192.

[19] PINHO C, MICÓ G, LIMA M, et al. Optimized design of Si_3N_4 structures for photonic integrated data compression applications[C]//2019 SBMO/IEEE MTT-S International Microwave and Optoelectronics Conference (IMOC), November 10-14, 2019, Aveiro, Portugal. New York：IEEE, 2019：1-3.

[20] SINGH S, RESNINA N, BELYAEV S, et al. Investigations on NiTi shape memory alloy thin wall structures through laser marking assisted wire arc based additive manufacturing[J]. Journal of manufacturing processes, 2021, 66：70-80.